Oct 1, 1993.

ANALYSIS OF AN AIRBORNE SAR INTERFEROMETER

S. Ponte^, G. Alberti°, S. Esposito°, A. Moccia^, S. Vetrella°

^Faculty of Engineering, University of Naples "Federico II"
P.le V. Tecchio, 80 - 80125 Napoli, Italy

°CO.RI.S.T.A., Consortium for Research on Advanced Remote Sensing Systems
P.le V. Tecchio, 80 - 80125 Naples, Italy

Abstract. This paper presents the analysis of C-band cross-track interferometric data (XTI) acquired by the TOPSAR system, on-board the NASA/JPL DC-8 aircraft, during the MAC Europe 1991 Campaign over the Matera test site (Southern Italy). The main technical aspects of interferometric processing, from raw data compression to DEM generation, have been addressed starting from the analysis of the collected raw data, compressed with a range-Doppler SAR processor which accounted for range migration effects and antenna squint. The phase difference map (interferogram) has been obtained after co-registration performed by using 1D cross-correlation techniques. The airplane attitude angles, recorded by the navigation system, have been used to derive the baseline time variation, necessary for the 2π ambiguity solving procedure. The ± 0.2 mm accuracy on the estimate of the baseline components gave a theoretical rms error on the height of ± 2.5 m for distributed targets, and ± 4.5 m for point targets. Finally, the computed terrain elevation has been compared with the 1:25,000 scale digitised contour levels of the Istituto Geografico Militare Italiano (IGMI), in order to assess the height accuracy of the system. The rms errors on the height estimate have been found to be ± 15 m for point targets, and ± 8 m for extended targets.

Introduction and basic principles

One of the most interesting applications of the interferometer principle combined to Synthetic Aperture Radar (SAR) technique is the possibility of reconstructing terrain heights by means of highly precise knowledge of distance, obtained from phase difference measurements. Radar interferometry is a promising technique which shows the potentiality of satisfying common medium and small-scale mapping requirements (Leberl 1990), in alternative and integration with the photogrammetric methods of topographic mapping. Besides the well-known advantages of active microwave remote sensing over passive imaging systems, such as all-weather and day-night capability, quick coverage, surface penetration potentiality, independence of resolution from the distance to the target, multi-polarization facilities, cross-track SAR interferometry offers 3D mapping capabilities satisfying various scientific requirements (Topographic Science Working Group 1988). Airborne InSAR systems have been used to create Digital Elevation Models (DEMs, Fig. 1).

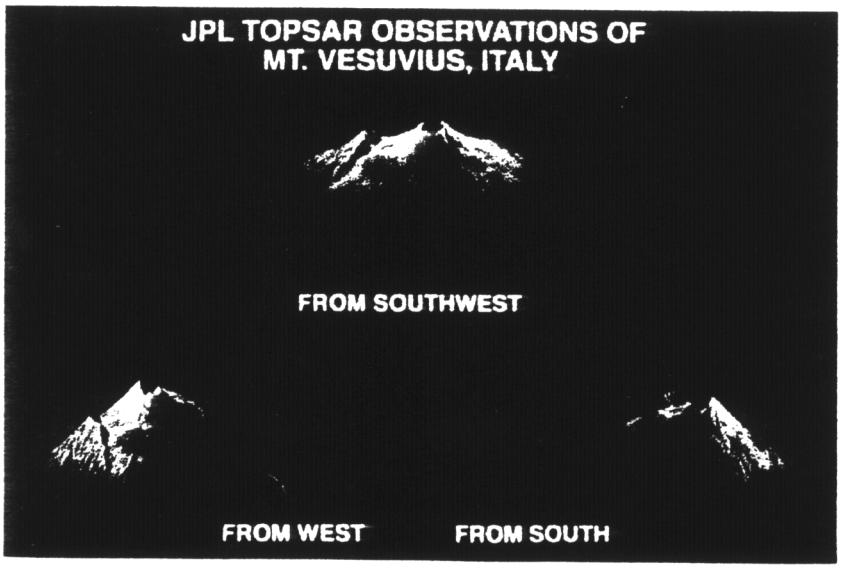

Fig. 1. TOPSAR DEM of Mount Vesuvio, Italy (courtesy of JPL).

High-resolution terrain elevation maps have been obtained either by analysing existing spaceborne and airborne systems, capable of producing multiple-pass interferometric pairs (Gabriel and Goldstein 1988 for SIR-B, Prati *et al.* 1990 for Seasat, Gray and Farris-Manning 1993 for the CCRS SAR-580), or by means of two antennas mounted on the same platform (Graham 1974 for Goodyear Aerospace (now Loral Defense System), Zebker and Goldstein 1986 for the NASA CV-990 radar, Madsen *et al.* 1993a for the NASA/JPL TOPSAR instrument).

The basic principle of one-pass airborne cross-track SAR interferometry is depicted in Fig. 2. One of the antennas is transmitting, and both are receiving. The backscattered echo returns from both antennas are collected and coherently added in one receiver, and a pair of conventional SAR images of the same scene is formed.

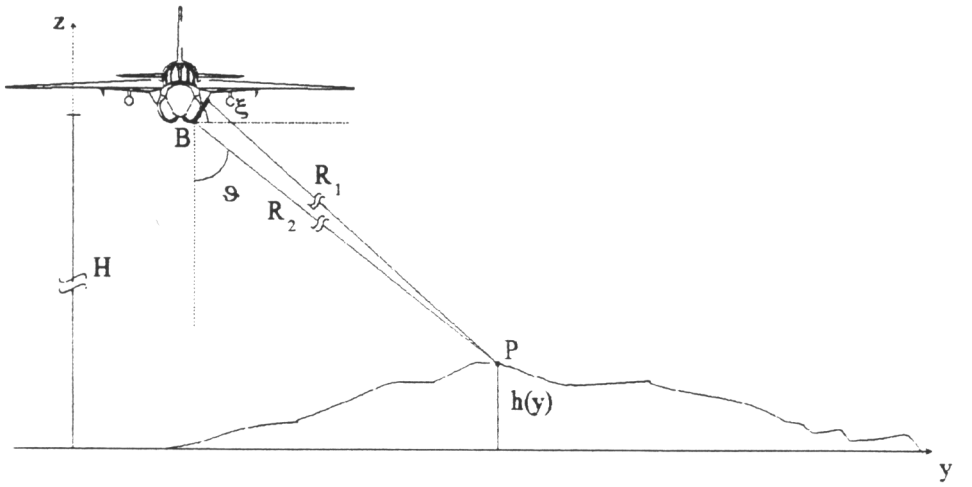

Fig. 2. Interferometric SAR geometry (flat Earth assumption).

An object point P will reradiate towards the receiving antenna pair, and the recorded signal will exhibit a phase difference $\Delta\phi$ related to the slant range difference $\Delta R=R_1-R_2$ as follows:

$$\Delta\phi = 2k\Delta R = \frac{4\pi}{\lambda}(R_1 - R_2)$$

where λ is the wavelength, R_1 and R_2 are the slant ranges from the two antennas to the imaged target, $k=2\pi/\lambda$ is the wavenumber and the factor 2 accounts for the two-way propagation path. It is possible to relate $\Delta\phi$ to the antenna separation vector (*baseline*), whose components in the cross-track plane are $B_y = B\cos\xi$, and $B_z = B\sin\xi$, with the following relation:

$$\Delta\phi = \frac{4\pi}{\lambda}\left(B_y \sin\vartheta - B_z \cos\vartheta\right)$$

where ϑ is the off-nadir, or look, angle and ξ is the baseline tilt angle. The phase information, therefore, depends on the baseline components, the baseline tilt angle, the slant range to the target, the look angle and the height of the imaged point, h(y). The surface topography h(y) is simply derived by the geometry of Fig. 2, under the assumption of flat Earth:

$$h(y) = H - R\cos\vartheta \qquad (1)$$

where H is the aircraft altitude.

Interferometric accuracies are limited in principle by radar wavelength and speckle effects, due to the coherent nature of the information gathered by the sensor (Li and Goldstein 1990). The phase errors also depend on the ground topography, in particular on the terrain slope. Too large slopes induce phase aliasing, and in the presence of layover or shadowing effects the phase information is either ambiguous or completely lost. Consequently, effective design of airborne and spaceborne InSAR systems requires to take into account the scene speckle correlation between the two passes, and the different geometries involved and the error sources affecting the phase information (see Rodriguez and Martin 1992 for a detailed description of the main design aspects of SAR Interferometry).

Currently, the Jet Propulsion Laboratory (JPL) under NASA contract, the University of Naples, Italy, and the Alenia Spazio under contract of the Italian Space Agency (ASI) are performing feasibility studies on a spaceborne InSAR for global topographic mapping, the Topographic Satellite (TOPSAT, Vetrella 1993). The design specifications exploit the main advantages of a satellite operating system, for example, the use of two spacecrafts operating simultaneously

to overcome temporal decorrelation problems, the improvement of the knowledge of the baseline by means of differential GPS techniques, and the use of low frequencies (L-Band) and low altitudes in order to improve the SNR.

This paper presents the analysis and the main results obtained from an operational airborne interferometric SAR, the Topographic Synthetic Aperture Radar (TOPSAR, Zebker *et al.* 1992), which has been used as an effective testbed to assess the reliability of the single-pass approach with respect to common problems in retrieving phase information in multiple-pass interferometry. During the multisensor airborne campaign MAC Europe 1991, C-Band cross-track interferometric (XTI) data were acquired over several test-sites, in order to verify the TOPSAR capability of delivering DEMs at great height accuracy and little spatial resolution. The authors focused their attention on Matera test-site (Basilicata, Southern Italy), where a set of active and passive calibration devices were deployed over a flat, homogeneous background. After a short description of the campaign, we present the main aspects of the coherent raw data focusing and the interferometric processing applied to obtain a DEM. In particular, the co-registration technique and the main considerations about the baseline estimation procedure and the related accuracy are outlined. The two-dimensional phase unwrapping algorithm is summarised, and a thorough error budget on the height estimate for both point and extended targets is carried out. Successively, the topographic mapping technique is verified by comparing the radar-derived DEM with the 1:25,000 scale digitised height points of the Italian Military Geographic Institute (IGMI), and characterising the rms difference between the heights for some deployed point targets as well as for some known extended targets in the imaged scene. Finally, some considerations on further developments and future research activity are presented.

1. The Matera interferometric experiment

On June 25, 1991, the TOPSAR instrument covered the Italian Matera test-site, gathering C-band cross-track interferometric data. The imaged area extends over about 130 km^2, and consists of prevailingly bare soil, well suited for sensor system evaluation, with slight changes of terrain height (50 m peak-to-peak, 15 m average). Ancillary ground information was collected by carrying out a simultaneous ground truth campaign, aimed at the classification of 50 sample areas and to the evaluation of texture, soil moisture content and surface roughness on sample points close to the location of 26 calibration devices with different Radar Cross-Sections (RCS) (CO.RI.S.T.A. 1991). The point targets were three Active Radar Calibrators (ARCs), jointly developed by CO.RI.S.T.A. and Polytechnic of Bari, Italy (Ponte *et al.* 1993), and 23 triangular trihedral Corner Reflectors (CRs), subdivided in 15, 5 and 3 with leg lengths of 95, 180 and 70 cm respectively.

Figure 3 shows the deployment scheme of CRs and ARCs on the test site, superimposed on the 1:25,000 scale IGMI map of the area, and the corresponding SAR image, in slant range-azimuth format. The two parallel lines of calibrators in the horizontal (ground range) direction were at a distance of 800 m with a spacing of 200 m between two adjacent CRs, to avoid coupling effects. The presence of calibrators allows the computation of a rectification grid based on many control points, well identified in the images to within two pixels. The point targets were deployed on a homogeneous background and positioned with electronic stadimeters and theodolites. The mean height of the calibrators' area was 370 m.

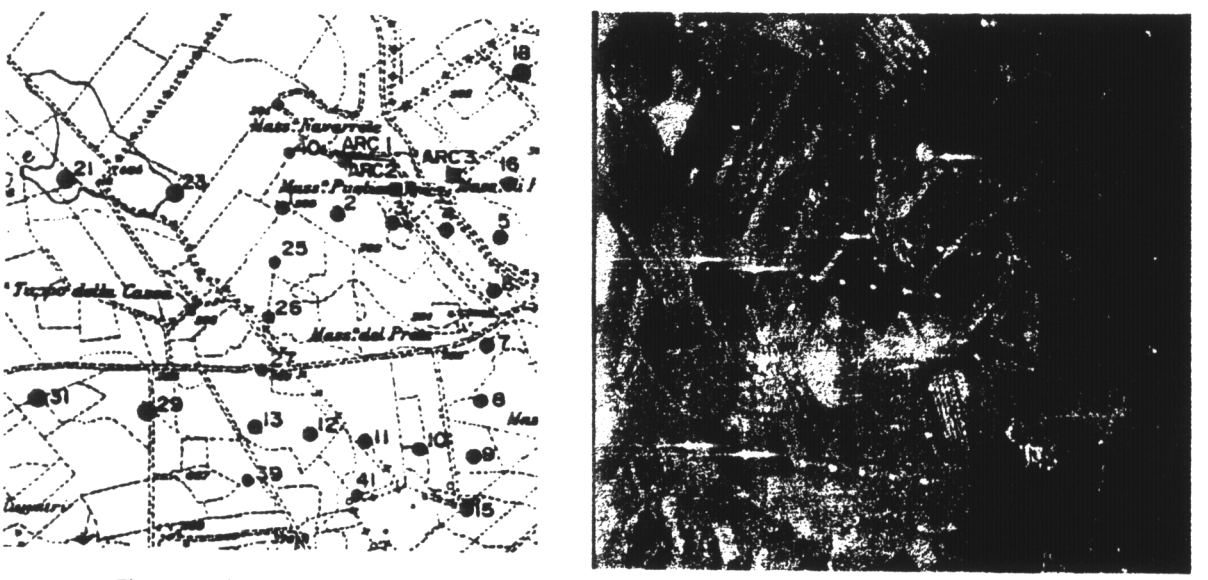

Fig. 3. Deployment scheme of active and passive calibrators, and corresponding SAR image of the area.

2. Raw data processing

Table 1 lists the main TOPSAR radar system parameters involved in raw data focusing (Zebker *et al.* 1992).

Frequency, wavelength	5.2873 GHz (C-band), 5.67 cm
Look angle, ϑ	from 30° to 60°
Flight altitude	~9 km
Aircraft speed	214.4 m/s
Swath width	4630 m (slant range)
Antenna length	1.6 m (along-track)
3-dB azimuth beamwidth	2°
Baseline modulus	2.583 m
Baseline tilt angle	62.77°
Slant range	11200 m (ϑ=45°)
Chirp bandwidth	40 MHz
Sampling frequency	90 MHz
Pulse length	5.0 μs
PRF	567 Hz
Ground range resolution	5.30 m (ϑ=45°)
Slant range resolution	3.75 m
Azimuth resolution	0.8 m (theoretical, 1 look)
SNR (point targets)	18 dB

Table 1. Main TOPSAR system parameters.

We have processed a frame of 16384 lines of 2700 range samples per line, centred on the calibrators' region, and the total imaged area has an extension of about 6x4.5 km^2. The data compression has been performed by means of a range-Doppler SAR processor which includes antenna squint correction and compensates the range migration effect, that is, the nonlinear fashion of the sensor-to-target distance during the formation of the synthetic aperture (Ulaby *et al.* 1982).

The channel imbalance has been removed by estimating the level of the calibration tone, injected into the receiver of the SAR system. Successively, a range migration analysis has been conducted on the responses of the range-compressed calibrators. The range lines of the image subset containing the visible "stripe" of the point target have been oversampled eight times by means of FFT techniques. In Fig. 4 the amplitude of the mainlobe peak value and the slant range to the target have been plotted as a function of the azimuth station.

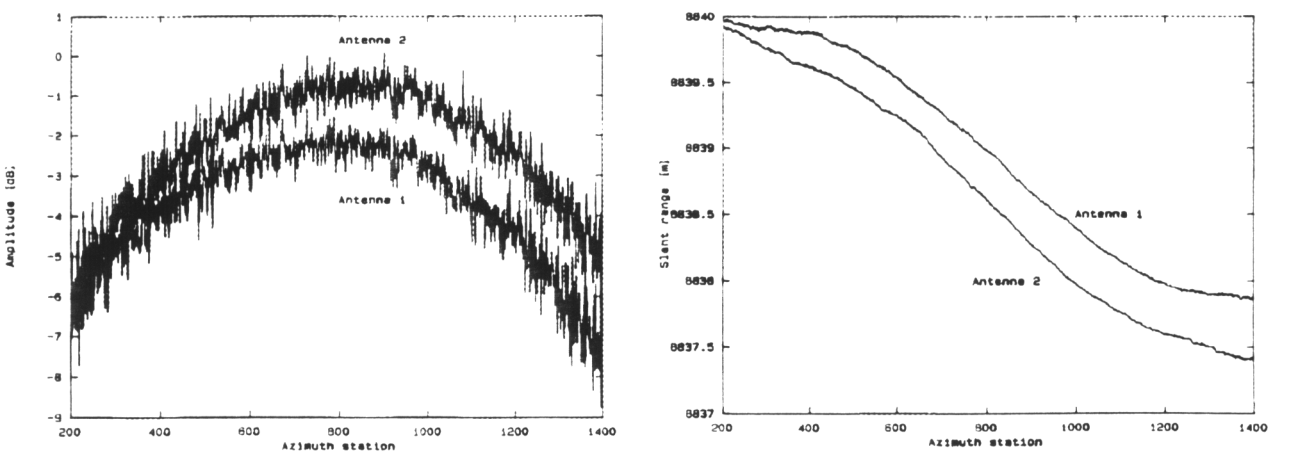

Fig. 4. Range migration analysis: (a) Position of the mainlobe peak value in the oversampled range-compressed image of a point target, and (b) Slant range history as a function of the azimuth position.

In Fig. 4 the channel imbalance (about 1 dB) and the tapering effect of the antenna azimuth pattern are clearly visible. A forward squint of the two antennas can be observed, whereas the slightly different shape of the range history of the same CR as seen by the antennas indicates the existence of a relative squint as well. This relative squint will lead to a

non perfect overlapping between the two images, and therefore to the need of image co-registration, as it will be shown in § 3.1.

The range migration (two pixels, about 7 m) and range walk (6÷8 m) derived from this analysis, are in agreement with the predicted range migration ($|\Delta r|$) and the theoretical range walk (r_w) given respectively by (Curlander and McDonough 1991):

$$|\Delta r| = \frac{\lambda R_0}{4\rho_{az}}\left(|\sin\vartheta_s| + \frac{\lambda \cos^2\vartheta_s}{8\rho_{az}}\right)$$

$$r_w = \frac{H\lambda\vartheta_s}{D\cos\vartheta}$$

where ρ_{az} is the azimuth resolution, D is the azimuth antenna length, ϑ_s is the antenna squint angle with respect to the nominal flight path (evaluated as shown later), and $R_0=H/\cos\vartheta$ is the slant range at the closest approach.

The corner-turned range-compressed data have been azimuth-processed in the frequency domain, estimating the Doppler centroid frequency with standard *clutterlock* techniques (Li *et al.* 1985). The squint angles of the two antennas, $\vartheta_{s,1}$ and $\vartheta_{s,2}$, have been derived from the clutterlock estimate of the Doppler centroid, f_{DC}, with the equation:

$$\vartheta_{s,i} = \sin^{-1}\left(\frac{\lambda f_{DC,i}}{2v}\right), \qquad i = 1,2$$

where v is the aircraft speed. The range migration correction has been performed in the frequency domain, reallocating the complex DFT coefficients along lines parallel to the azimuth direction. The adopted algorithm is based on 8-points cubic B-spline interpolation, and takes the Doppler frequency variation into account. The residual phase terms due to the antennas' squint have been corrected, and a Hamming weighting has been applied to the reference function.

In order to validate the processor performance, a set of standard image quality tests have been carried out. We evaluated the one-dimensional ground range and azimuth resolutions, the Integrated Sidelobe Ratio (ISLR) and the Peak Sidelobe Ratio (PSLR) on the point target responses (JPL SIR-C Team *et al.* 1990, Moccia *et al.* 1991), finding a mean broadening factor of 5% in ground range, and about 15% in azimuth. The mean value of the SNR for point targets has been found to be 18 dB.

3. Interferometric post-processing

3.1 Image co-registration

The aforementioned differences in the Doppler centroid frequencies for the two antennas caused a relative azimuth displacement in the final images, making therefore necessary the use of co-registration techniques. To this end, we applied a simple one-dimensional cross-correlation method. The cross-correlation function of the azimuth pixel amplitudes was oversampled by cubic B-spline techniques up to one tenth of pixel (<5 cm, see Table 1). The position of the peak correlation value gave the required offset for the corresponding azimuth line: on the basis of this offset, each line of one of the two images has been resampled by using an 8-points cubic B-spline interpolation function, which minimises the least-square error of the function value (Strang 1986).

After resampling, we multiplied one image by the complex conjugate of the co-registered image, to obtain the single-look interferogram, and successively a coherent multi-look of eight pixels in the azimuth direction has been performed, to carry out a maximum-likelihood estimate of the phase difference (Rodriguez 1992). The eight-looks interferogram is shown in Fig. 5: the fringes are quite parallel due to the flatness of the area, and the effects on the phases of the point targets with the strongest echo returns (CRs No. 21, 23, 29, 31, with leg length of 180 cm and RCS of 41.4 dBm^2; ARC No. 1, with RCS of 44.3 dBm^2) are visible.

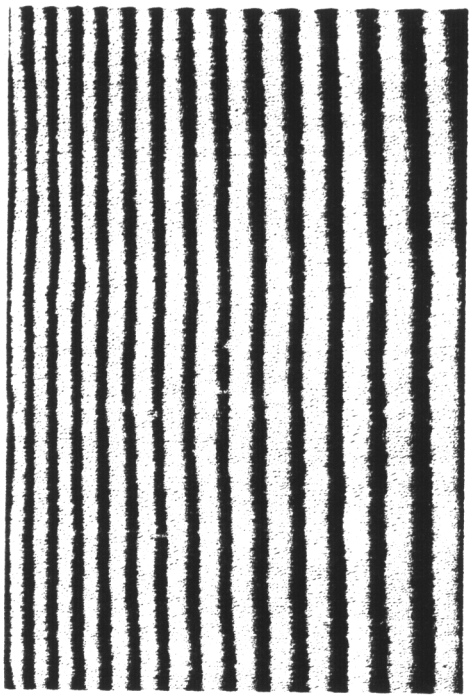

Fig. 5. Eight-look interferogram of the processed area.

3.2 Estimate of the baseline components and related accuracy

The interferometer sensitivity and noise properties are mainly affected by the baseline length, the wavelength and the distance from sensor to target. Moreover, the accurate knowledge of the phase centre of the two antennas allows one to improve the terrain height estimation accuracy. The estimation of the TOPSAR baseline components, which depend on the aircraft attitude dynamics, is a crucial point when reconstructing the off-nadir angle from the slant range and the phase differences of the interferogram (*phase unwrapping*) and when converting the fringe map, or phase surface, into absolute height measurements (Li and Goldstein 1990).

The attitude data relative to the processed frame have been extracted from the header file associated to the collected raw data. The ancillary information was given by the Digital Avionic Data system (DAD) and the radar inertial navigation system (LASERREF) on-board the aircraft, and it allowed us the analysis of platform motion. Table 2 reports a statistical analysis of pitch, yaw and roll angles, recorded by the LASERREF system at a 50 Hz update rate, with a quantization precision of 0.01 degrees. The attitude peak-to-peak variations during the analyzed frame have been found to be about 0.25°.

Attitude angles [deg]	Mean value	St. deviation
Yaw	0.408	0.063
Pitch	1.465	0.069
Roll	-0.418	0.064

Table 2. Statistics of the attitude angles relative to the processed data segment.

By using these average estimates, and assuming a yaw-pitch-roll rotation sequence, we applied a co-ordinate transformation to express the baseline components in a right-handed dynamic reference frame, with the origin coincident with the Inertial Navigation Unit (INU) position, the z-axis coincident with the local vertical and directed towards the Earth, and the y-axis perpendicular to the plane defined by the INU velocity vector and the local vertical (Moccia and Vetrella 1986). The co-ordinate transformation matrix between the dynamic and the body-fixed reference frame (origin coincident with the INU and axes parallel to the aircraft inertia principal axes), $\mathbf{M}_{ypr}$, is given by:

$$\mathbf{M}_{ypr} = \begin{vmatrix} \cos\beta\cos\gamma & -\cos\alpha\sin\gamma + \sin\alpha\sin\beta\cos\gamma & \sin\alpha\sin\gamma + \cos\alpha\sin\beta\cos\gamma \\ \cos\beta\sin\gamma & \cos\alpha\cos\gamma + \sin\alpha\sin\beta\sin\gamma & -\sin\alpha\cos\gamma + \cos\alpha\sin\beta\sin\gamma \\ -\sin\beta & \sin\alpha\cos\beta & \cos\alpha\cos\beta \end{vmatrix} \qquad (2)$$

where α, β and γ are the roll, pitch and yaw angles, respectively, and $\mathbf{B}_0 \equiv (B_{0x}, B_{0y}, B_{0z})$ is the baseline vector in the

body-fixed reference frame. Table 3 reports the baseline components with respect to the body-fixed reference frame, and the estimated ones in the dynamic reference frame, whereas the two reference frames are shown in Fig. 6.

	Body-fixed ref. frame	Dynamic ref. frame
$\|B\|$ [m]	2.5823	
B_x [m]	$x_{02}-x_{01}=0.000$	$x_2-x_1=0.0541$
B_y [m]	$y_{02}-y_{01}=-1.1821$	$y_2-y_1=-1.1991$
B_z [m]	$z_{02}-z_{01}=-2.2969$	$z_2-z_1=-2.2876$
ξ [deg]	62.77	62.34

Table 3. Baseline components in the body-fixed and dynamic reference frames.

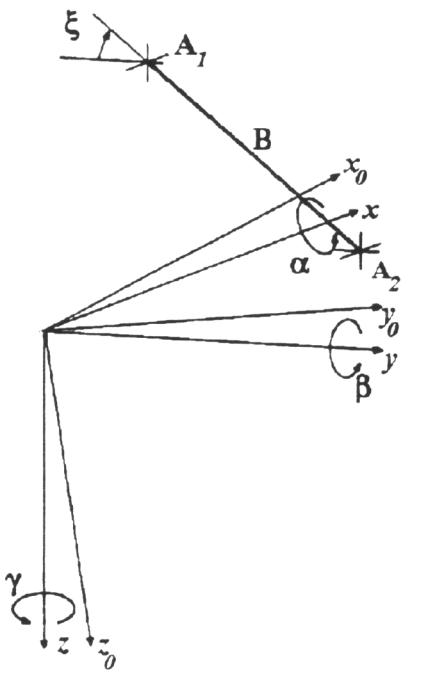

Fig. 6. Dynamic and body-fixed reference frames, with the baseline orientation: A_1 and A_2 represent the antennas' positions.

Assuming uncorrelated fluctuations in the observations of the attitude angles, and using Eq. (2), under the hypothesis of small angles, we derived the variances of the baseline components in the dynamic reference frame, $\sigma^2_{B_x}$, $\sigma^2_{B_y}$, $\sigma^2_{B_z}$, as a function of the variances of the attitude angles, σ^2_α, σ^2_β, σ^2_γ. In matrix notation:

$$\begin{vmatrix} \sigma^2_{B_x} \\ \sigma^2_{B_y} \\ \sigma^2_{B_z} \end{vmatrix} \cong \begin{Vmatrix} 0 & B^2_{z_0} & B^2_{y_0} \\ B^2_{z_0} & 0 & B^2_{x_0} \\ B^2_{y_0} & B^2_{x_0} & 0 \end{Vmatrix} \begin{vmatrix} \sigma^2_\alpha \\ \sigma^2_\beta \\ \sigma^2_\gamma \end{vmatrix}$$

where $B_{x0}=x_{02}-x_{01}$, $B_{y0}=y_{02}-y_{01}$ and $B_{z0}=z_{02}-z_{01}$, are the nominal baseline components (Table 3). The variances σ^2_α, σ^2_β, σ^2_γ are of the order of 10^{-8} rad^2. With these values, the accuracy on the baseline components estimation was of the order of ± 0.2 mm.

3.3. Reconstruction of absolute phase information and DEM generation

The estimated baseline components (Table 3) have been used to extract from the interferogram the information on terrain elevation. After having chosen one of the deployed calibrators (CR No. 2) as a GCP (Ground Control Point) of known height and distance from the radar, the 2π ambiguity has been solved, and the integration of the phase

difference (*phase unwrapping*) has been carried out. We implemented a procedure based on edge detection techniques to locate the fringe lines in the interferogram (Lin *et al.* 1992), an effective method which solved satisfactorily the phase indetermination problem. In Fig. 7 the original interferogram with the edge-enhanced fringe lines, i. e. the boundaries of the 2π-addition on the integrated phase, is shown, and a cut of the phase surface from near to far range, after the edge-enhancement procedure is plotted in Fig. 8.

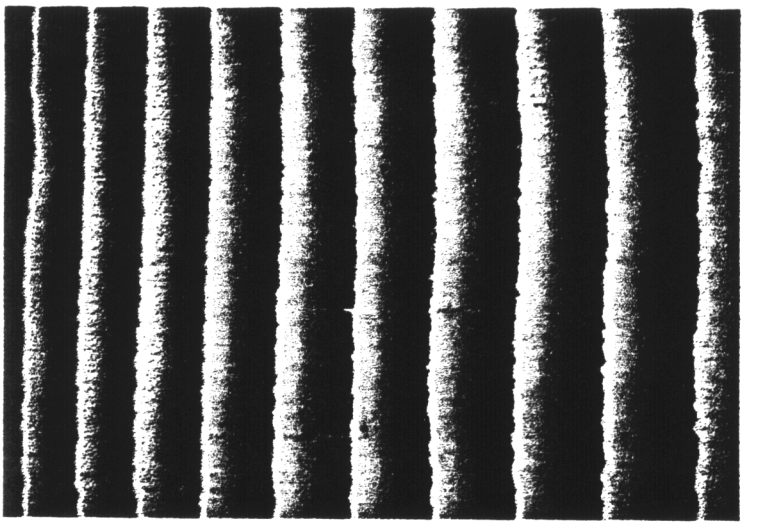

Fig. 7. Edge-enhanced fringe lines.

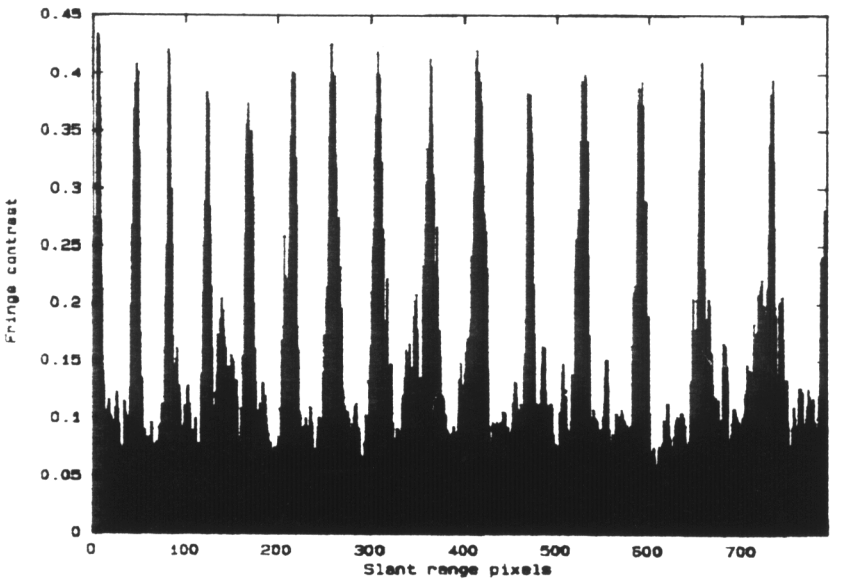

Fig. 8. Fringe contrast after edge enhancement.

The fringe contrast η has been evaluated as:

$$\eta = \frac{1}{2\pi MN} \sum_{i=1}^{M} \sum_{j=1}^{N} \left| \phi_{ij} - \overline{\phi} \right|$$

where $\phi_{ij} \in [-\pi, \pi[$ is the phase value of a pixel of an inspection matrix with M rows and N columns, and $\overline{\phi}$ is the mean value of the M·N complex elements of the matrix. The selected values of M and N were 9 and 7 respectively. These values satisfy a symmetry criterion (an equal number of pixels on the sides of the fringe line, bounded within two pixels) and are well suited with respect to the estimated vertical and horizontal distances between two adjacent null lines, or fringes. In correspondence of a null line, $\overline{\phi}$ is close to 0, whereas the deviations $\left| \phi_{ij} - \overline{\phi} \right|$ are close to π: therefore, the fringe contrast has high values (≥ 0.4) when crossing a phase-inversion line.

The unwrapping algorithm worked very well, and there were little or no mislocations of fringe lines due to phase

noise. In fact, the degree of coherence between the two images and the SNR were very high, and the number of residue regions (areas of inconsistent phase unwrapping) was negligible. At this point, by using the computed baseline components and the unwrapped phase information, we were able to derive a DEM. The height *h* of a pixel has been computed using Eq. (1), and the slant range to the pixel has been evaluated with respect to the slant range of the GCP. The look angle was evaluated from the estimated phase difference $\Delta\phi$ and the baseline tilt angle ξ by inverting the following equation:

$$\Delta\phi = \frac{2\pi}{\lambda}\left[\frac{B_{yz}^2}{2R}\sin^2(\xi-\vartheta) + B_{yz}\sin(\xi-\vartheta) - \frac{B^2}{2R}\right] \tag{3}$$

where $B_{yz}^2 = B_y^2 + B_z^2$ is the projection of the baseline vector on the y-z plane. It is worth noting that the detection of fringe lines with edge enhancement techniques was insensitive to the effect of the strongest point targets on the phases. The null line detection and the consequent unwrapping were correctly performed, whereas a first attempt of solving the 2π ambiguity, based on the identification of residues and the creation of branch cuts to identify areas of inconsistency of the phase integration (Goldstein *et al.* 1988), had shown an unacceptable error propagation in the pixel regions located near the strong point target calibrators.

4. Estimating the height from the phase difference: theoretical error budgets

This section briefly outlines the approach followed for a theoretical evaluation of the contributions of various error sources in the estimation of the pixel elevation from the analysis of the phase difference contained in the interferogram. The principal error-affected parameters are the aircraft altitude, the slant range knowledge, the estimated look angle, and the baseline components. Further details can be found in Li and Goldstein 1990.

4.1. Rms height error for point targets

Deriving an error budget of the height estimate when the imaged pixel is representative of the echo return of a point target is useful for system transfer function evaluation (Moccia and Vetrella 1992). Considering only the strong received phasor with no decorrelation effects, if *h* is the pixel elevation, and $\Delta\phi$ is the estimated phase difference between two homologous pixels (Eq. (3), applied after image co-registration), the basic equations for computing the topographic information are (Fig. 2):

$$\begin{cases} \Delta R = \dfrac{\lambda}{2\pi}\Delta\phi = \dfrac{B_{yz}^2}{2R}\sin^2(\xi-\vartheta) + B_{yz}\sin(\xi-\vartheta) - \dfrac{B^2}{2R} \\ h = H - R\cos\vartheta = H - R\left(\sqrt{1-\beta^2}\cos\xi - \beta\sin\xi\right) \\ \beta = \sin(\xi-\vartheta) = \dfrac{(R+\Delta R)^2 - R^2 - B^2}{2RB} \end{cases}$$

where ΔR is the path difference. Assuming uncorrelated parameters, the height measurement uncertainty σ_h^2 is given by:

$$\sigma_h^2 = \left(\frac{\partial h}{\partial H}\right)^2\sigma_H^2 + \left(\frac{\partial h}{\partial R}\right)^2\sigma_R^2 + \left(\frac{\partial h}{\partial \vartheta}\right)^2\sigma_\vartheta^2 + \left(\frac{\partial h}{\partial B_x}\right)^2\sigma_{B_x}^2 + \left(\frac{\partial h}{\partial B_y}\right)^2\sigma_{B_y}^2 + \left(\frac{\partial h}{\partial B_z}\right)^2\sigma_{B_z}^2 \tag{4}$$

where σ_H is the aircraft altitude uncertainty, σ_R represents the uncertainty in the sampling time of the echo return (it is of the order of 30 cm because it depends on the internal clock accuracy), σ_ϑ is the uncertainty on the look angle, and σ_{Bx}, σ_{By}, σ_{Bz}, the baseline components uncertainties, have been derived from the aircraft attitude dynamics. Simple algebra leads to the following expression for the derivative terms in Eq. (4):

$$\frac{\partial h}{\partial H} = 1$$

$$\frac{\partial h}{\partial R} = -\cos\vartheta$$

$$\frac{\partial h}{\partial \vartheta} = R\sin\vartheta$$

$$\frac{\partial h}{\partial B_x} = \frac{1}{q} B_x \sin\vartheta$$

$$\frac{\partial h}{\partial B_y} = \frac{p}{q} B_y \sin\vartheta$$

$$\frac{\partial h}{\partial B_z} = \frac{p}{q} B_z \sin\vartheta$$

$$p = \frac{R}{B_{yz}} \sin(\xi - \vartheta) - \cos^2(\xi - \vartheta)$$

$$q = B_{yz} \cos(\xi - \vartheta) \left[1 + \frac{B_{yz}}{R} \sin(\xi - \vartheta) \right]$$

The uncertainty on the measured phase difference, which induces an uncertainty σ_ϑ on the measured look angle, is related to the variance of the quantization error on $\Delta\phi$. Expressing σ_h^2 as a function of the baseline length, a quadratic form is obtained:

$$\sigma_h^2 = K + C \left[\frac{R \tan(\xi - \vartheta) - B\cos(\xi - \vartheta)}{RB + B^2 \sin(\xi - \vartheta)} \right]^2 \qquad (5)$$

where:

$$K = \sigma_H^2 + \cos^2\vartheta \sigma_R^2 + R^2 \sin^2\vartheta \sigma_\vartheta^2$$

$$C = R^2 \sin^2\vartheta \sigma_B^2$$

Eq (5) has been derived assuming $B \equiv B_{yz}$, because the uncertainty on B_x, of the order of 10^{-4}, has been neglected with respect to the uncertainties σ_{By} and σ_{Bz}, of the order of 10^{1}.

4.2. Rms height error for distributed targets

For a distributed target whose backscattering coefficient is $\sigma^0(x,y,z)$, viewed at ϑ radians, it can be shown (Rodriguez and Martin 1992) that γ, the correlation coefficient between the interferometric echo returns v_1 and v_2, is given by:

$$\gamma = \frac{\left| \langle v_1 v_2^* \rangle \right|}{\sqrt{\langle |v_1|^2 \rangle \langle |v_2|^2 \rangle}} = \frac{|\alpha|}{1 + R_{SN}^{-1}}$$

where R_{SN} is the system SNR, and α is given by:

$$|\alpha| = \left(1 - \frac{\rho_{az} B_x}{R_0 \lambda} \right) \left(1 - \frac{\rho_{sr} B_y}{R_0 \lambda \sin\vartheta} \right) \cdot w\left[\frac{\delta_x}{\rho_{az}} \left(1 - \frac{\rho_{az} B_x}{R_0 \lambda} \right), \frac{\delta_r}{\rho_{sr}} \left(1 - \frac{\rho_{sr} B_y}{R_0 \lambda \sin\vartheta} \right) \right] \cdot \frac{\mathcal{F}\{\sigma^0\}_{(x,y,a)}}{\sigma^0(x,y,z)}$$

where B_x and B_y are the along-track and cross-track baseline components, respectively, δ_x and δ_y are the azimuth and range offsets between the two images, $w(x,y)$ is the impulse response function, which has been chosen to be given by a two-dimensional *sinc* function. The operator $\mathcal{F}\{\bullet\}$ represents the Fourier transform of σ^0, evaluated in (x,y,a), where a is equal to $-B\cos(\xi-\vartheta)/R_0\lambda\sin\vartheta$. The uncertainty on the phase difference, $\sigma_{\Delta\phi}$, is derived by applying the Cramer-Rao

bound on the estimator of $\Delta\phi$ from an N_L-looks image (Rodriguez 1992):

$$\sigma^2_{\Delta\phi} = \frac{1}{2N_L}\frac{1-\gamma^2}{\gamma^2}$$

to be applied in Eq. (3) to derive the height error budget for distributed targets. A plot of Eq. (5) is shown in Fig. 9, obtained using a value of ±0.2 mm for the uncertainty on the baseline components, ±1 m for the uncertainty on aircraft altitude, and with 45° incidence angle (mid swath). Considering a baseline length of 2.58 m, the expected height error is ±4.5 m for point targets and ±2.7 m for distributed targets. The SNR values adopted are 18 dB for point targets (13 dB for distributed targets), whereas the standard deviation of the quantization error, σ_q, was set to $1.7 \cdot 10^{-4}/\sqrt{12}$ radians.

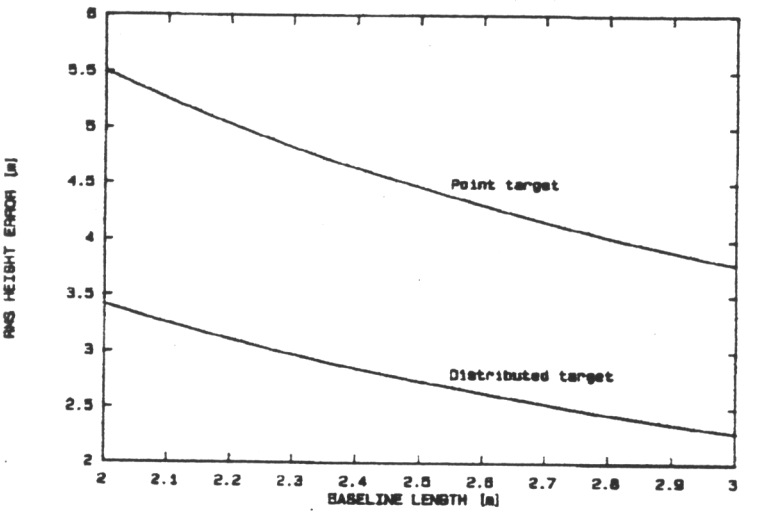

Fig. 9. Theoretical error budget on the height estimate.

5. DEM validation through comparison to existing digital height maps

The DEM of the area under study, after the removal of systematic errors by using the known GCP's height, was evaluated by performing a comparison with the digitised scattered height-points sampled by IGMI. The radar-derived DEM, in slant range-azimuth format, is shown in Fig. 10.

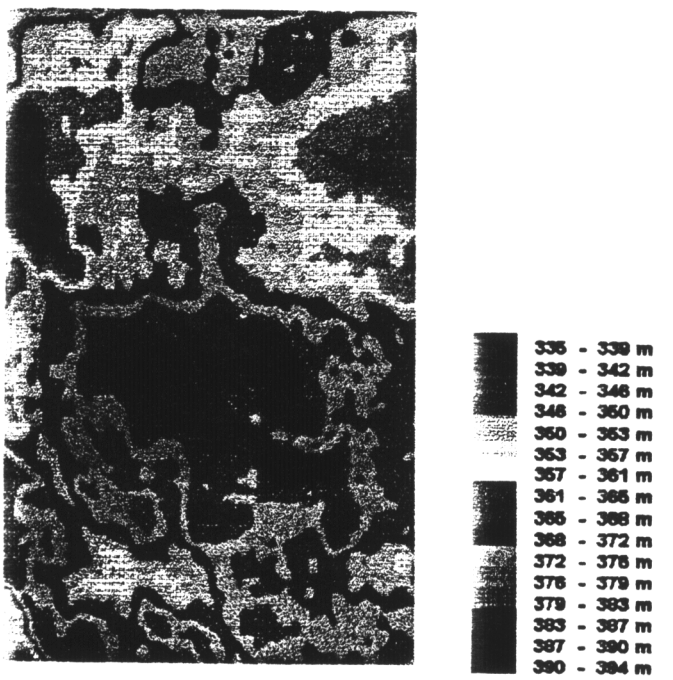

Fig. 10. Radar-derived DEM of the processed area.

The IGMI height points have an accuracy of ±3 m at 1:25,000 scale. The DEM in raster format was obtained from the original elevation points by means of a computer code (Vetrella and Moccia 1988). Currently, no rectification of the radar-derived height map has been implemented, and studies on co-registration between radar DEMs and reference DEMs are being performed. Nevertheless, it has been possible to verify the quality of the height map obtained by means of interferometry, on the basis of the knowledge of elevation and position of the CRs and ARCs deployed on the test-site. We chose fifteen CRs to carry out an analysis of the difference between the true height value and the computed elevation: the root-mean-square value of this difference has been found to be about 15 m, which is more than 200% greater than the predicted theoretical value (see Fig. 9). Fig. 11a shows the height values in both cases, from the radar-derived map and from the reference DEM, and Fig. 11b plots the differences between the two heights.

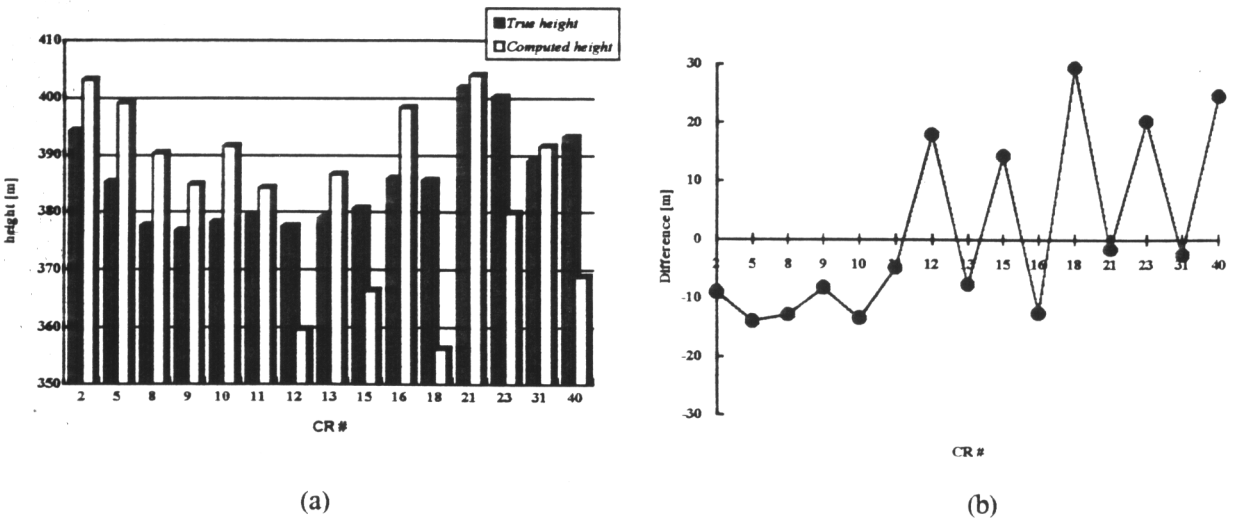

(a) (b)

Fig. 11. (a) Height values from the radar-derived and the reference DEMs. (b) Difference between true and computed heights on the 15 analyzed CRs.

In order to make use of extended targets in the validation of our DEM, we cut eight areas of 15x15 pixels (representative of an area of about 2.000 m^2), large enough to be considered representative of a distributed target, and sufficiently small to assume the incidence angle constant over the whole region. The analysis of the rms difference gave us an estimate of the rms height error for uniform areas. The cuts were close to the positions of the selected CRs, but without including their responses, and they have been chosen and located on the IGMI DEM as flat areas. From the results shown on Fig. 12, the mean rms value of the difference between true and computed heights is ±8.1 m, about 200% greater than the theoretical error budget.

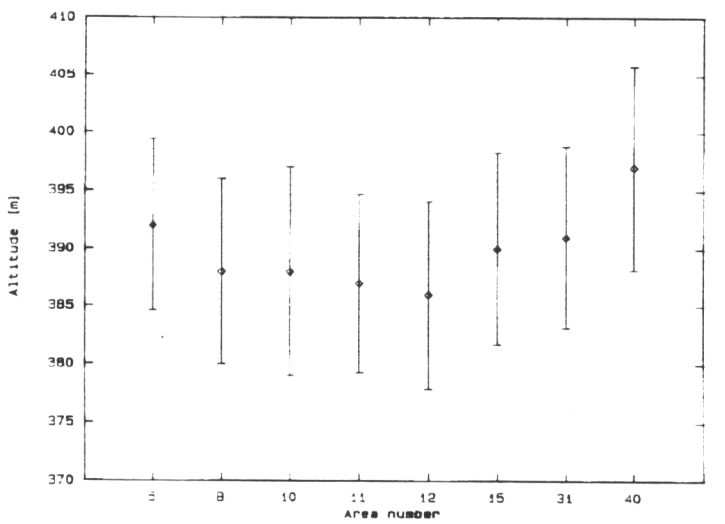

Fig. 12. Analysis on eight distributed areas surrounding some CRs. The errorbars represent the rms error on the estimated height.

The quality results on the radar DEM show that motion compensation is mandatory, in order to optimise the performance of the end-to-end InSAR processing chain. By reconstructing the displacement history of the antenna phase center with respect to a reference track, it is possible to calculate a slant-range dependent phase correction for each range-compressed pixel (Madsen *et al.* 1993a). The compensation of spurious phase terms will enable us to evaluate the phase information as if the antenna travelled along a straight line with constant speed. Motion compensation is the major issue of our future work in airborne interferometric SAR processing.

Conclusions and further developments

We have presented the analysis and the main results of the TOPSAR experiments conducted in 1991 in Southern Italy, devoted to assess the TOPSAR capability to produce high-quality DEMs. By using a SAR processor developed by CO.RI.S.T.A., the interferometric raw data collected by the two channels have been focused separately, and an interferogram of an area on which several point targets were deployed has been derived. After co-registration of the images, which had a relative squint angle of 0.2°, we estimated the baseline time-varying components from the header data relative to the processed frame, and we performed a fringe-enhancement procedure by means of edge detection algorithms to correctly unwrap the phase information. The DEM obtained from the XTI SAR data has been validated by computing the height rms error with respect to the IGMI digitised elevation points of the test site. This procedure has been applied to a set of homogeneous areas, as well as to a set of 15 point targets, which height was known after a ground truth campaign. The theoretical error analysis for both point and extended targets has shown rms values of the height accuracy less than the values found on the TOPSAR DEM.

The primary improvement to be performed in our interferometric processing is the development of motion compensation algorithms. With a very accurate knowledge of aircraft position, velocity and attitude, it will be possible to estimate and remove the additional error contributions to the interferometric phase due to the platform motion. In addition, the atmospheric corrections seem to play an important role in the absolute accuracy requirements (Madsen *et al.* 1993b), together with the need of state-of-the-art reference DEMs, in order to perform the phase calibration of a SAR interferometer, and to validate motion compensation algorithms. Work is currently underway in "de-biasing" the on-board INU data relative to vertical accelerations and position, to obtain correct reference terms which could improve the phase unwrapping technique, by means of a better knowledge of the altitude.

A further promising motion compensation technique that we are presently analysing consists in the determination of the aircraft trajectory and altitude by making use of the phase histories of the point targets. In this case, the time-varying antenna-target distances allow one to compute the antenna position and velocity vector components in an Earth-fixed reference frame, by using least squares approximations. Of course, this technique has its major limitation in the availability of strong and precisely located point targets within the area under study. Nevertheless, it can be used to validate and/or integrate on-board ancillary data, giving results which can be extrapolated to the whole trajectory.

Finally, further activity is required in order to implement co-registration techniques between available reference DEMs, converted to raster format, and rectified interferometric DEMs, either by using arrays of corner reflectors, as done by Madsen *et al.* 1993 with the TOPSAR data sets gathered during the 1992 experiments at Ft. Irwin, or by estimating geometric distortions such as misalignment, skew or slope errors. An airborne interferometric SAR simulator, which is currently being developed and tested, could be a useful tool in studying, evaluating and simulating sensor errors, target mislocation, foreshortening and layover effects, and processor-induced geometric distortions. The main objective is an automated procedure to map the SAR image into a rectified, ground-range format, compensated for terrain and processing effects.

Acknowledgements

This activity has been carried out under the sponsorship of the Italian Space Agency (ASI). The use of the digitised elevation points has been authorised by the Istituto Geografico Militare Italiano (IGMI, Auth. No. 3759 29/1/1993).

References

CO.RI.S.T.A., 1991, Progetto SAR 1991: Rapporto Finale Campagna Agrisar. A report prepared by AQUATER SpA. CO.RI.S.T.A. internal document 004/92.

CURLANDER, J. C., and MCDONOUGH, R. N., 1991, Synthetic Aperture Radar. Systems and Signal Processing (New York: John Wiley & Sons, Inc.)

GABRIEL, A. K, and GOLDSTEIN, R. M., 1988, Crossed orbit interferometry: theory and experimental results from SIR-B. International Journal of Remote Sensing, Vol. 9, No. 8, pp.857-872.

GOLDSTEIN, R. M., ZEBKER, H. A., and WERNER, C. L., 1988, Satellite radar interferometry: two-dimensional phase unwrapping. Radio Science, Vol. 23, No. 4, pp. 713-720.

GRAHAM, L. C., 1974, Synthetic Interferometer Radar For Topographic Mapping. Proceedings of the IEEE, Vol. 62, No. 6, pp. 763-768.

GRAY, A. L., FARRIS-MANNING, P. J., 1993, Repeat-Pass Interferometry with Airborne Synthetic Aperture Radar. IEEE Transactions on Geoscience and Remote Sensing, Vol. 31, No. 1, pp. 180-191.

JPL SIR-C TEAM, DLR NE-HF X-SAR TEAM, I-PAF X-SAR TEAM, 1990, Data products and image quality assessment for the SIR-C/X-SAR mission, Version 1.0. JPL Document D-7193.

LEBERL, F. W., 1990, Radargrammetric Image Processing (Norwood, MA: Artech House, Inc.).

LI, F. K., HELD, D. N., CURLANDER, J. C., and WU, C., 1985, Doppler Parameter Estimation for Spaceborne Synthetic-Aperture Radars. IEEE Transactions on Geoscience and Remote Sensing, Vol. GE-23, No. 1, pp. 47-56.

LI, F. K., and GOLDSTEIN, R. M., 1990, Studies of Multibaseline Spaceborne Interferometric Synthetic Aperture Radars. IEEE Transactions on Geoscience and Remote Sensing, Vol. 28, No. 1, pp. 88-97.

LIN, Q., VESECKY, J. F., ZEBKER, H. A., 1992, New Approaches in Interferometric SAR Data Processing. IEEE Transactions on Geoscience and Remote Sensing, Vol. 30, No. 3, pp. 560-567.

MADSEN, S. N., ZEBKER, H. A., MARTIN, J., 1993a, Topographic Mapping Using Radar Interferometry: Processing Techniques. IEEE Transactions on Geoscience and Remote Sensing, Vol. 31, No. 1, pp. 246-256.

MADSEN, S. N., MARTIN, J., and ZEBKER, H. A., 1993b, Analysis and Evaluation of the Performance of the TOPSAR Interferometer. This same workshop.

MOCCIA, A., VETRELLA, S., 1986, An integrated approach to geometric precision processing of spaceborne high-resolution sensors. International Journal of Remote Sensing, Vol. 7, No. 3, pp. 349-359.

MOCCIA A., and VETRELLA, S., 1992, A Tethered Interferometric Synthetic Aperture Radar (SAR) for a Topographic Mission. IEEE Transactions on Geoscience and Remote Sensing, Vol. 30, No. 1, pp. 103-109.

MOCCIA, A. VETRELLA, S., and PONTE, S., 1991, Passive and Active Calibrators Characterization by using a Spaceborne SAR System Simulator. Proc. of the SAR Calibration Workshop, DLR, Oberpfaffenhofen, Germany, October 9th-11th, 1991.

PONTE, S., POSA, F., SCHENA, V., VETRELLA S., 1993, MAC Europe 1991 Campaign: Design and Performance Evaluation of an Active Radar Calibrator (ARC). Presented at the CEOS Workshop on SAR Calibration, ESA/ESTEC, Nordwijk, The Netherlands, September 20th-24th, 1993.

PRATI, C., ROCCA, F., MONTI GUARNIERI, A., and DAMONTI, E., 1990, Seismic Migration for SAR Focusing: Interferometrical Applications. IEEE Transactions on Geoscience and Remote Sensing, Vol. 28, No. 4, pp. 627-640.

RODRIGUEZ E., 1992, Maximum likelihood estimation of the interferometric phase from distributed targets. IEEE Transactions on Geoscience and Remote Sensing, to be published.

RODRIGUEZ, E., MARTIN, J. M., 1992, Theory and design of interferometric synthetic aperture radars. IEE Proceedings, Vol. 139, No. 2, pp. 147-159.

STRANG, G., 1986, Introduction to applied mathematics (Wellesley, MA: Wellesley-Cambridge Press), pp. 177-180.

TOPOGRAPHIC SCIENCE WORKING GROUP, 1988, Topographic Science Working Group Report to the Land Processes Branch, Earth Science and Applications Division, NASA Headquarters. Lunar and Planetary Institute, Houston, 64 pp.

ULABY, F. T., MOORE, R. K., FUNG, A. K., 1982, Microwave Remote Sensing, Active and Passive. Vol. II: Radar remote sensing and surface scattering and emission theory (London: Addison-Wesley Publishing Company).

VETRELLA, S., 1993, Global Topography Mission (GTM) Overview. Presented at the International Workshop on SAR Interferometry, Naples, Italy, May 18-20, 1993.

VETRELLA, S., and MOCCIA, A., 1988, A Procedure for Modeling the Terrain Relief by Using Digitized Topographic Maps. Geocarto international, Vol. 3, No. 3, pp. 3-11.

ZEBKER, H. A., MADSEN, S. N., MARTIN, J., WHEELER, K. B., MILLER, T., and LOU, Y., ALBERTI, G., VETRELLA, S. and CUCCI, A., 1992, The TOPSAR Interferometric Radar Topographic Mapping Instrument. IEEE Transactions on Geoscience and Remote Sensing, Vol. 30, No. 5, pp. 933-940.

ZEBKER, H. A., and GOLDSTEIN, R. M., 1986, Topographic Mapping From Interferometric Synthetic Aperture Radar Observations. Journal of Geophysical Research, Vol. 91, No. B5, pp. 4993-4999.